Energy Storage Materials 76 (2025) 104112

Contents lists available at ScienceDirect

Energy Storage Materials

journal homepage: www.elsevier.com/locate/ensm

Sodium storage of -Sn/TiO_2/Sn/TiO_2- Superlattice heterojunctions

Xueyi Lu [a,1], Weixin Chen [a,1], Jianfang Yang [a], Xuemin Wu [a], Yan Wang [b], Oliver G. Schmidt [c,d], Lifeng Liu [e,f,*], Daiming Tang [g,*], Xia Lu [a,*]

[a] School of Materials, Sun Yat-sen University, Shenzhen 518107, PR China
[b] Guangdong Provincial Key Laboratory of Materials and Technologies for Energy Conversion, Guangdong Technion-Israel Institute of Technology, Daxue Road 241, Shantou 515063, PR China
[c] Research Center for Materials, Architectures and Integration of Nanomembranes (MAIN), TU Chemnitz, Chemnitz 09126, Germany
[d] International Institute for Intelligent Nanorobots and Nanosystems (IIINN), Fudan University, Shanghai, PR China
[e] Songshan Lake Materials Laboratory (SLAB), Dongguan 523808, PR China
[f] International Iberian Nanotechnology Laboratory (INL), Braga 4715-330, Portugal
[g] Research Center for Materials Nanoarchitectonics (MANA), National Institute for Materials Science, Namiki Tsukuba Ibaraki 305-0044, Japan

ARTICLE INFO

Keywords:
Heterostructural electrochemistry
Built-in electric field
-Sn/TiO_2/Sn/TiO_2- heterojunctions
sodium storage

ABSTRACT

Electrochemistry of heterostructures plays a fundamental role in developing high-performance energy storage and conversion devices. However, current superlattice heterostructures based on assembling 2D materials are limited to a small number of alternating units with weak interfacial interaction and ambiguous function mechanism. Herein, the high-order -Sn/TiO_2/Sn/TiO_2- (S/TO) superlattice heterojunctions with built-in electric fields (BIEFs) are designed for sodium storage using a strain release method. The results show that the accommodated BIEFs and the spatial confinement effect in this periodic nanostructured electrode co-contribute to the outstanding electrochemical performance. The nanosizing and pulverization of Sn are effectively space-limited in between the TiO_2 slabs and the notorious catalytic reaction between electrolyte and TiO_2 surface region is sophisticatedly mitigated by the electron accumulation in the TiO_2 component, synergistically accelerating sodium storage and transfer kinetics of S/TO superlattice electrodes. The covalent Sn-O-Ti interactions further enhance the robustness to sustain repeated (de)sodiation processes. These findings provide a rewarding avenue towards the development of high-performance electrodes by heterostructural electrochemistry.

1. Introduction

Electrochemical energy storage systems, including lithium-ion batteries (LIBs) [1], sodium-ion batteries (SIBs) [2], supercapacitors [3], have attracted continuous research interest as key components in portable electronics and electric vehicles. In particular, SIBs with similar working principle as LIBs exhibit substantial promise for use in stationary energy storage and even in electric vehicles due to the huge abundance of Na in nature, the favorable specific capacity with respect to $LiFePO_4$-based LIBs and the manufacturing process compatible with current existing LIBs manufacturing processes [4–6]. In present SIBs, the electrode materials determine the performance of batteries to a great extent while actually there are still many challenges to get an expected electrochemical performance by improving the known positive/-negative materials [7]. Taking the important anode materials as example, a variety of materials have been investigated for SIBs, such as hard carbon [8], tin [9,10], transition metal phosphide [11], MXene [12], oxides [13,14], and chalcogenides [8,15,16], each having its own pros and cons that restrict it from achieving optimal performance. For instance, tin-based materials exhibit a high specific capacity but their cycle stability is unsatisfactory because of their severe volume changes during discharge/charge. By comparison, titanium oxide (TiO_2) presents a low specific capacity though its cycle stability is outstanding [17–19].

Recently, the design of heterojunctions composed of distinct components has emerged as a highly effective strategy to fully leverage their respective advantages and enhance electrochemical energy storage capabilities [20–22]. In particular, the fabrication of vertical superlattice heterostructures based on 2D materials with sequential stacks allows them to complement each other effectively and gives birth to new physical and chemical properties, thus improving the sodium storage

* Corresponding authors.
E-mail addresses: liu.lifeng@sslab.org.cn (L. Liu), TANG.Daiming@nims.go.jp (D. Tang), luxia3@mail.sysu.edu.cn (X. Lu).
[1] X. Y. Lu and W. Chen contributed equally to this work.

https://doi.org/10.1016/j.ensm.2025.104112
Received 15 December 2024; Received in revised form 26 January 2025; Accepted 7 February 2025
Available online 8 February 2025

performance beyond what could be achieved independently [23,24]. In this respect, Guo and coworkers stacked complementary 2D materials to fabricate a phosphorene/MXene superlattice anode for stable and fast sodium storage, not only alleviating the structural expansion of phosphorene, but also spurring the electron migration with superior cycling performance (343 mAh g^{-1} after 1000 cycles at 1 A g^{-1}) [25]. Wang et al. reported a superlattice comprised of alternatively restacked defective $Ti_{0.87}O_2$ and N-doped graphene nanosheets for sodium storage, which exhibits a high specific capacity of ~490 mAh g^{-1} at 0.1 A g^{-1} and a reversible Na^+ intercalation process without phase and structural change [26]. Of special interest is that adjustable BIEFs can be introduced into the heterogeneous interfaces which play an important role in optimizing the electrochemical performance of hybrid materials [27–29]. We have ever created BIEFs within the superlattice heterostructures by electrostatic assembly of unilamellar $TiNbO_5$ and graphene nanosheets as building blocks, enabling an excellent reversible sodium storage capacity of 245 mAh g^{-1} [14]. Theoretical analysis confirmed that such BIEFs can enhance the electric conductivity and facilitate electron transfer at the atomic interface.

Despite tremendous progress, there still exist limitations of current superlattice materials for sodium storage. Regarding the synthesis strategies, the co-synthesis strategy rarely considers the static properties and interface compatibility of the stacks. The weak interlayer interaction of Van der Waal (vdW) force can not sustain the repeated (de) intercalation processes. In terms of more established superlattice heterostructures (*e.g.,* 0D/2D, 1D/2D), they can not provide continuous and simultaneous ionic/electronic diffusion pathways due to the presence of interstices within the components. On the other hand, the 2D nanosheet superlattices prepared by electrostatic assembly are limited to a small number of blocks because of the mismatched lateral sizes of different nanosheets and the uncontrollable electrostatic attractions that tend to generate disordered networks instead of the strictly face-to-face alternate restacks. Worse still, the composites consist of disparate nanosheets with approximate thickness and unaligned edges which usually makes it very difficult to characterize the superlattice structure from the cross-section view. In addition, the controversial functional mechanism of superlattices in energy storage deserves in-depth and comprehensive understanding [29]. In general, the dimensionality, composition and interfaces of superlattice heterojunctions exert considerable influence on charge separation, mass and electron transfer, consequently affecting their electrochemical activity in SIBs. Therefore, it is of great scientific importance to rationally design superlattice heterostructures and unveil the functional mechanism of sodium ion storage to build better SIBs.

In this work, a facile strain-release approach is implemented to fabricate -Sn/TiO_2/Sn/TiO_2- high-order thin film superlattice heterostructures, consisting of alternated units of metallic Sn and TiO_2 layers with the precisely engineered interfaces and modulated BIEFs. As one type of two-dimensional materials, thin films offer attractive merits in metallic ion storage, including well-controlled thicknesses, versatile combination of chemical composition and excellent mechanical elasticity, *etc.* [30–33]. The stacking hybridization of thin films not only makes full use of the high specific capacity of Sn but also overcomes its shortcoming in large volume change through spatial confinement by TiO_2 layers. More intriguingly, upon the formation of heterostructures, the unbalanced surface charge densities of Sn and TiO_2 induces BIEFs across the heterointerface as confirmed by scanning Kelvin probe microscopy (SKPM). Density functional theory (DFT) calculations also illustrate the electron transfer from Sn to TiO_2, which results in the positive and negative charged surface of Sn and TiO_2, respectively and constructures BIEFs which effectively facilitated the electronic and ionic transfer during Na^+ intercalation and deintercalation processes. In addition, the cross-linking Sn-O-Ti covalent interactions endow the heterointerface special robustness that cannot be obtained in vdW heterostructures, which enabled them to sustain repeated (de)sodiation, thus helping to deliver a much higher specific capacity and stability.

2. Results and discussion

2.1. Preparation and characterization of S/TO superlattice heterojunctions

The S/TO heterojunctions were synthesized by physical evaporation combined with the self-assembly of rolled-up thin films [34,35]. Briefly, as schematically illustrated in Fig. 1a, the photoresist was first spin coated onto the substrate (Al foil) as the sacrificial layer (SL), followed by the alternate deposition of metallic Sn and TiO_2 thin films in a vacuum e-beam evaporator. Afterwards, the substrate coated with the hybrid thin films was immersed into isopropanol to etch away the photoresist layer. Owing to the built-in strain, the hybrid thin films roll up into a tubular structure automatically and detach from the substrate (Figure S1). These free-standing thin film tubes are then dried by a super critical dryer to maintain their intact structures (Figure S2). As shown in Fig. 1b, the 2D planar S/TO nanomembranes transform to 3D tubular structures with compact multilayered walls characterized by scanning electron microscopy (SEM). The energy-dispersive X-ray spectroscopy (EDS) mapping verifies the homogeneous distribution of Sn, Ti and O in the hybrid structure (Fig. 1c). The phase composition was examined by X-ray diffraction (XRD). The typical diffraction peaks at 30.7°, 32.0°, 43.9°, 62.7°, 64.7° and 64.9° correspond to (200), (101), (220), (211), (112) and (321) planes of metallic Sn (PDF#04–0673) while those peaks at 25.3°, 37.1°, 37.8°, 38.7°, 48.1°, 53.8° and 68.9° are precisely indexed as the anatase TiO_2 (PDF#21–1272) (Fig. 1d). By calculating the lattice mismatch between metallic Sn and anatase TiO_2, there is a value lower than 2.4 % to indicate the high degree of matching for building the S/TO heterojunctions according to Tables S1–2. Further Raman spectroscopy results reveal that although the metallic Sn thin films exhibit no Raman signals, there are still five peaks with Raman shifts of 150, 196, 396, 516 and 638 cm^{-1}, corresponding to E_g, E_g, B_{1g}, A_{1g} and E_g modes of anatase TiO_2 as shown in Figure S3 [36]. The S/TO thin films resemble similar signals but with lower intensity, which could be ascribed to the confinement effect of Sn on the surface of TiO_2 surface.

The embedded S/TO heterojunctions present an ordered spatial arrangement, where the hybrid S/TO thin films are composed of alternate Sn and TiO_2 as inspected by SEM and transmission electron microscopy (TEM) in Fig. 2a and S4–6. The thicknesses of Sn and TiO_2 slabs are measured to be ~ 30 and 15 nm, respectively. Of special interest is that there exists abundant crosslinked structures and pores (labeled by yellow loops and red lines) at the interfaces (ranging from 5 to 10 nm), which suggests the newly constructed interfacial Sn-O-Ti bonds upon the formation of heterostructures as shown in Fig. 2b. In the high-resolution TEM images, *d*-spacings of 0.29 and 0.35 nm are detected, corresponding to the Sn (200) and TiO_2 (101) planes as shown in Fig. 2c, d. The energy dispersive X-ray spectroscopy (EDS) and X-ray spectroscopy (XPS) survey show the spatial distribution and chemical states of Pt, Ti, O and Sn elements in the corresponding stacks in Fig. 2e-i and S7–8. For Ti 2p XPS spectrum shown in Fig. 2j, the TiO_2 exhibits a peak at a binding energy of 458.5 eV which blue-shifts to 458.8 eV in the S/TO heterojunctions, which is highly correlated with the formation of Sn-O-Ti interfacial bonds. The Sn-O-Ti bonds will weaken the shift of covalent electrons towards O and lower the binding energy of O 1 s (529.9 to 529.6 eV) in the S/TO as shown in Fig. 2k. Such interfacial structures and bonding state polarize partial electron transfer from O to Sn and weakens the intrinsic Ti-O covalent bonds, on the contrary, form the Sn-O bonds (486.6 eV), thus enhancing the binding energy of Ti 2p bonds (485.5 to 458.8 eV) as shown in Fig. 2j-l. Moreover, in the Sn 3d spectrum of pure Sn thin film, the XPS peaks with binding energies of 484.5 and 486.6 eV are ascribed to the metallic Sn and SnO phases, respectively, as revealed in Fig. 2l [37]. It can be seen that the surface of ultrathin Sn slabs tends to be oxidized although the Sn is protected by TiO_2, again demonstrating the formation of Sn-O-Ti interfacial bonds to build the -Sn/TiO_2/Sn/TiO_2- heterojunctions.

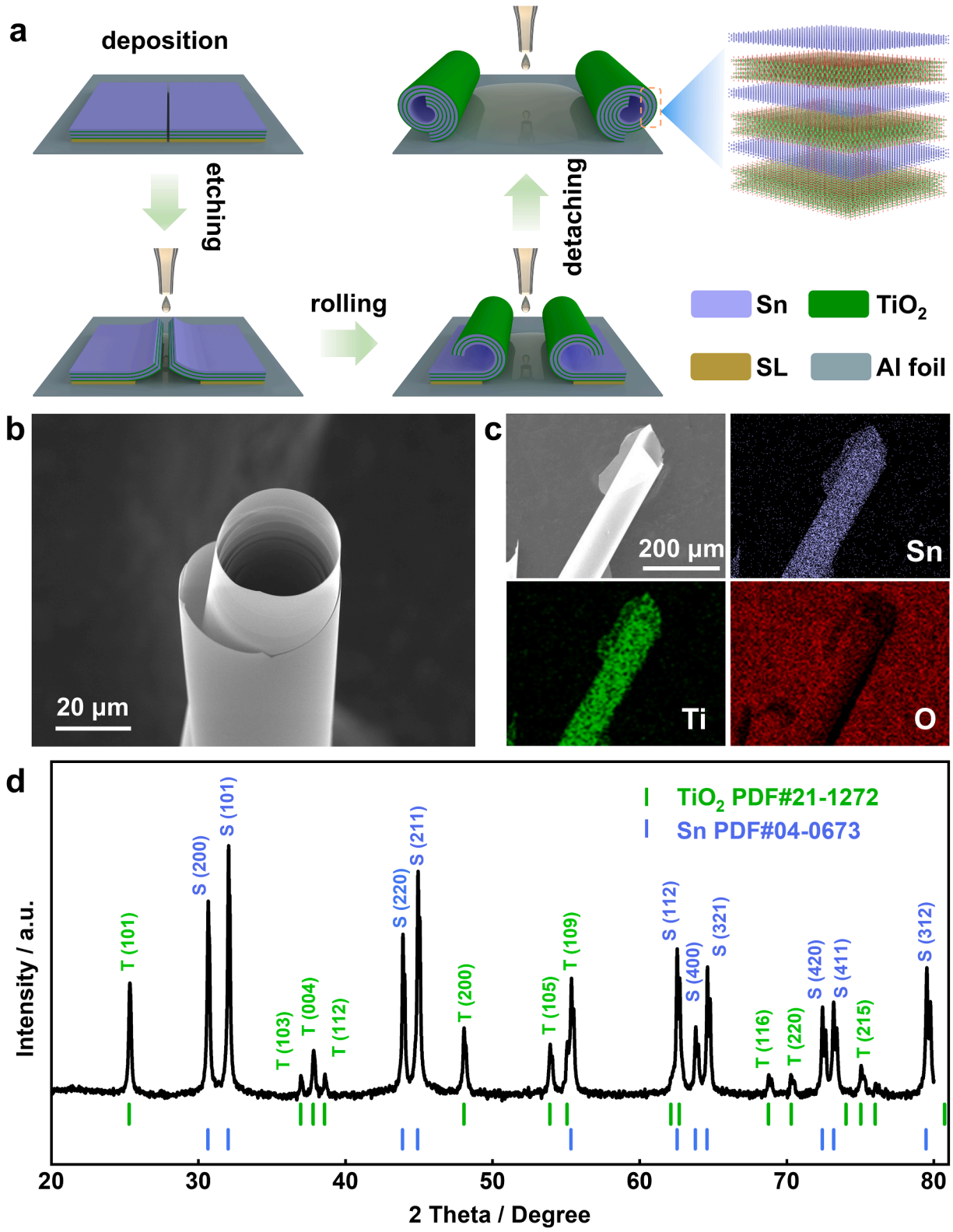

Fig. 1. Fabrication and characterization of S/TO heterojunctions. (a) Schematic illustration of the fabrication process; (b, c) SEM images and elemental mappings of S/TO thin films; (d) XRD pattern of S/TO thin films.

Furthermore, a stepped TiO_2/Sn heterojunction was built to examine the BIEFs as shown in Fig. 3 and S9. SKPM is employed to analyze the BIEFs by probing the potential difference on the TiO_2/Sn heterojunction. For the SKPM test, the TiO_2 thin film was first coated on the Si substrate followed by depositing patterned Sn thin film arrays via a micro-nano fabrication process. The height difference (~ 18 nm) indicates the successful deposition of Sn on the TiO_2 slab to construct the TiO_2/Sn stepped stacks as presented in Fig. 3a, c and S10–11. Accordingly, the measured potential difference between TiO_2 and Sn is ~ 15 mV (Fig. 3b, d). Consequently, the calculated BIEFs is ~10^3 V/m along the direction

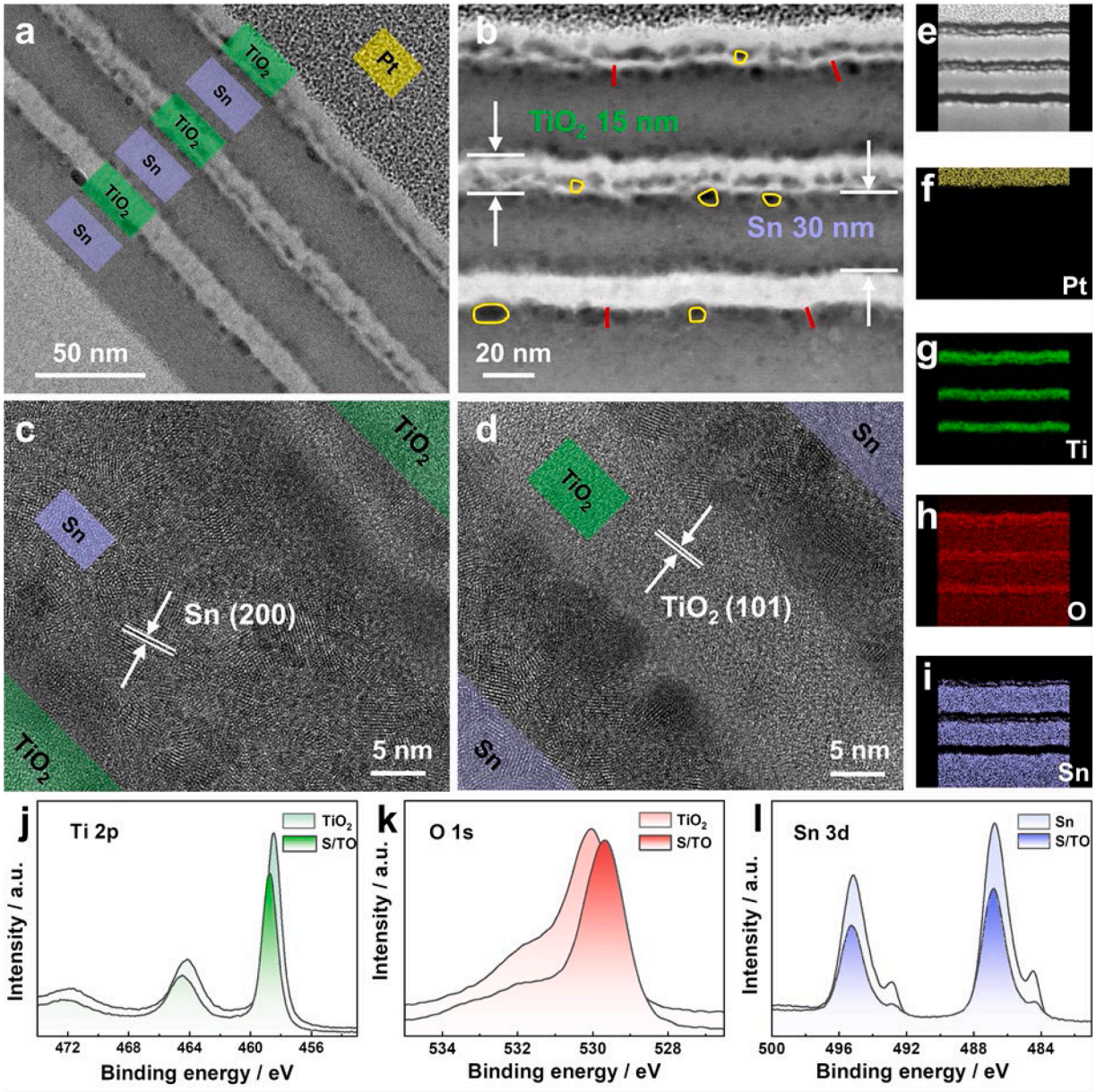

Fig. 2. Morphology of S/TO heterojunctions. (a, b) TEM images where the interfacial pores and Sn-O-Ti bonds are labeled by yellow loops and red lines, respectively. (c, d) HR-TEM images, where each slab is composed of abundant nanoparticles. (e-i) Elemental mappings of S/TO. (j-l) High-resolution Ti 2p, O 1 s and Sn 3d XPS spectra.

from Sn to TiO_2 slabs across the heterojunctions, where the width of interfacial region is ~10 nm as shown in Fig. 1b. Such potential reveals the directed electron migration from Sn to TiO_2 slab upon the formation of heterostructures, where, as a matter of fact, the elongation or shrinkage of Ti-O bonds plays a key role in generating the electron capturing or releasing centers [38,39]. It is interesting that the electric conductivity of TiO_2 slab is significantly enhanced upon the generation of Sn-O-Ti interfacial bonds in the heterojunction region, which would be beneficial for the sodium uptake and electrons shift and may significantly improve the electrochemical performance.

2.2. Electrochemical performance of S/TO thin films

The electrochemical performance of S/TO multi-heterojunctions, Sn and TiO_2 thin films were investigated in sodium batteries. Fig. 4a and S12 display the galvanostatic discharge-charge profiles of the three different electrode materials acquired at 0.05 A g^{-1}. The Sn and TiO_2 thin films deliver specific discharge capacities of 1646 and 1307 mAh g^{-1} in the first cycle with low enough Coulombic efficiencies of 28.3 % and 12.1 %, respectively. Such a lower Coulombic efficiency can be firstly ascribed to the intrinsic open structure and extremely high specific surface areas which consume as much electrolyte and Na^+ ions as possible to construct the electrode-electrolyte interphases (mainly the SEI and the surface/interface defects). When it comes to the S/TO heterojunction electrode, it presents a higher specific capacity of 1750 mAh g^{-1} with a Coulombic efficiency of 22.7 %. There is a plateau at ~ 0.7 V in the discharge curve, corresponding to the sodiation of TiO_2 [40]. The following plateaus at ~ 0.5 and 0.3 V can be attributed the sequential alloying steps of Sn with Na [41]. The following sodiation corresponds to the surface-redox behaviors and formation of irreversible electrode-electrolyte interphases. In the charge curve, the initial several plateaus are ascribed to the de-alloying processes followed by the desodiation of TiO_2. As shown in Figure S13, the battery delivers a specific capacity of 1229 mAh g^{-1} at 0.05 A g^{-1} with a higher S/TO mass

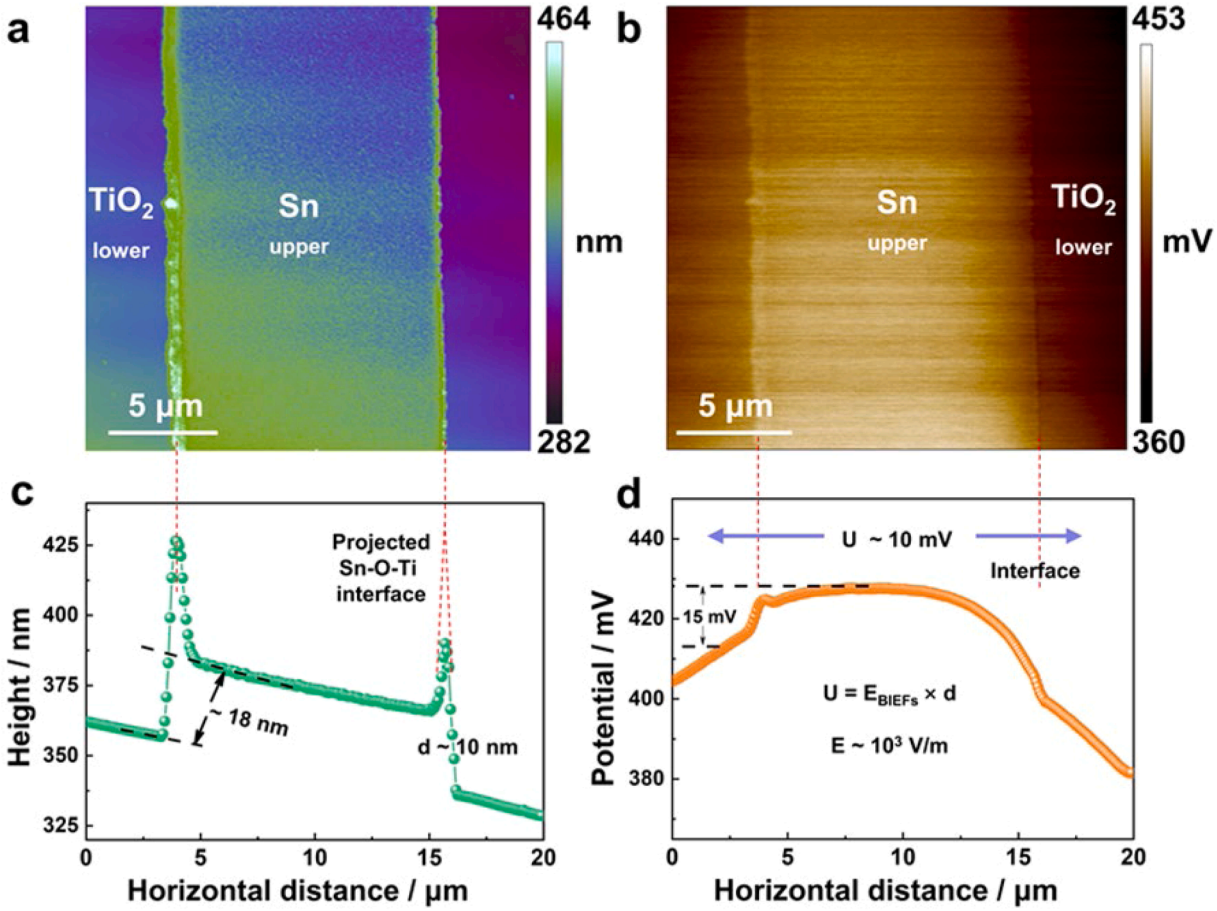

Fig. 3. Built-in electric fields in metal (Sn)/semiconductor (TiO_2) heterojunctions. (a, b) SKPM top view images, where the upper narrow layer is the metal Sn slab and lower wide layer corresponds to the TiO_2 slab. (c) Corresponding height and (d) potential profiles of the Sn/TiO_2 heterojunctions.

loadings of 2.0 mg cm^{-2} . The battery also experiences an active process and achieves a specific capacity of 502 mAh g^{-1} at the 50th cycle, approaching that with a lower mass loading. To be specific, the S/TO electrode experiences an activation process and eventually achieve a much higher specific capacity of 513 mAh g^{-1} than Sn (315 mAh g^{-1}) and TiO_2 (178 mAh g^{-1}) after 50 cycles, which approaches the theoretical value (Table S3). Moreover, as shown in Figure S14, the Sn-TiO_2 physical mixture delivers a specific capacity of 1437 mAh g^{-1} and a Coulombic efficiency of 31.1 %. Due to a higher exposure of TiO_2, the physical mixture exhibits more obvious intercalation process of TiO_2 at ~ 0.75 V than that of the S/TO while the capacity degrades severely during cycling, illustrating the function of BIEFs in enhancing sodium storage performance.

The following rate capability of S/TO electrode reveals specific capacities of 513, 409, 356, 312, 267 and 224 mAh g^{-1} at various current densities from 50 to 100, 200, 300, 500 and 1000 mA g^{-1} as shown in Fig. 4b and S15, obviously higher over the single-component Sn and TiO_2 electrodes. An apparent concerted effect can be conducted in the S/TO electrode, where the generated Sn-O-Ti interface structure and the introduced BIEFs functionalize the storage and transport of Na^+ and also stabilize the heterojunction structure to ensure the rate and long cycling performance. From the galvanostatic intermittent titration technique (GITT) measurement (Figure S16), the diffusion coefficient is measured to be around 10^{-12} cm^2 s^{-1} for Na^+ ion diffusion inside the S/TO multi-heterojunctions, higher than that of Sn (~ 10^{-15}–10^{-16} cm^2 s^{-1}) and TiO_2 (~ 10^{-14}–10^{-15} cm^2 s^{-1}), further verifying the contribution of BIEFs to accelerate the Na^+ ion diffusion. The electrochemical impedance spectroscopy (EIS) shows that the battery with S/TO heterojunctions exhibits a small Ohmic resistance (Figure S17). Fig. 4c presents the long-term cycling stability of different thin film electrodes at a higher current density of 1.0 A g^{-1}. The S/TO electrode perfectly inherits the high specific capacity of Sn electrode and the cycling stability of TiO_2 electrode, delivering a specific capacity of 229 mAh g^{-1} even after 2000 cycles which is 3.1 and 6.0 times that of Sn and TiO_2 materials (Fig. 4c and S18), which also greatly exceeds the Sn and TiO_2 based materials reported in the literatures (Table S4). Such a deliberate design of S/TO heterostructures firstly employ the confinement effect of TiO_2 on both sides of Sn to suppress the volume change and exfoliation of Sn nanoparticles during the repeated sodiation/desodiation processes. In turn, the coated Sn layers on both sides of TiO_2 not only enhance the conductivity but also effectively retard the catalytic activity of Ti ions to the electrolyte to stabilize the storage and cycling performance. The covalent interaction via Sn-O-Ti further enhances the robustness of superlattices during the long-term cycling. The cycled Sn and S/TO thin film electrodes were characterized by SEM to analyze their structural changes. It can be seen that the pure Sn thin film presents debris and crack morphology while most of the S/TO heterojunction sustains the relative decent tubular structure (Figure S19), justifying that the TiO_2 slabs could effectively prohibit the structural changes of Sn by space-confinement effect. The sodium ion full cells have been assembled with S/TO anode and $NaVPO_4$ (NVP) cathode, delivering the high charge and discharge specific capacities of 112 and 97 mAh g^{-1} at 0.05 A g^{-1} (Figure S20).

Next, a detailed analysis of the obtained specific capacity of the S/TO electrode is conducted, where it generally includes two processes, viz. the faradaic contribution controlled by ionic diffusion and charge transfer-controlled faradaic contribution, and the nonfaradaic electrochemical double-layer effect [42]. The diffusion-capacitive kinetics

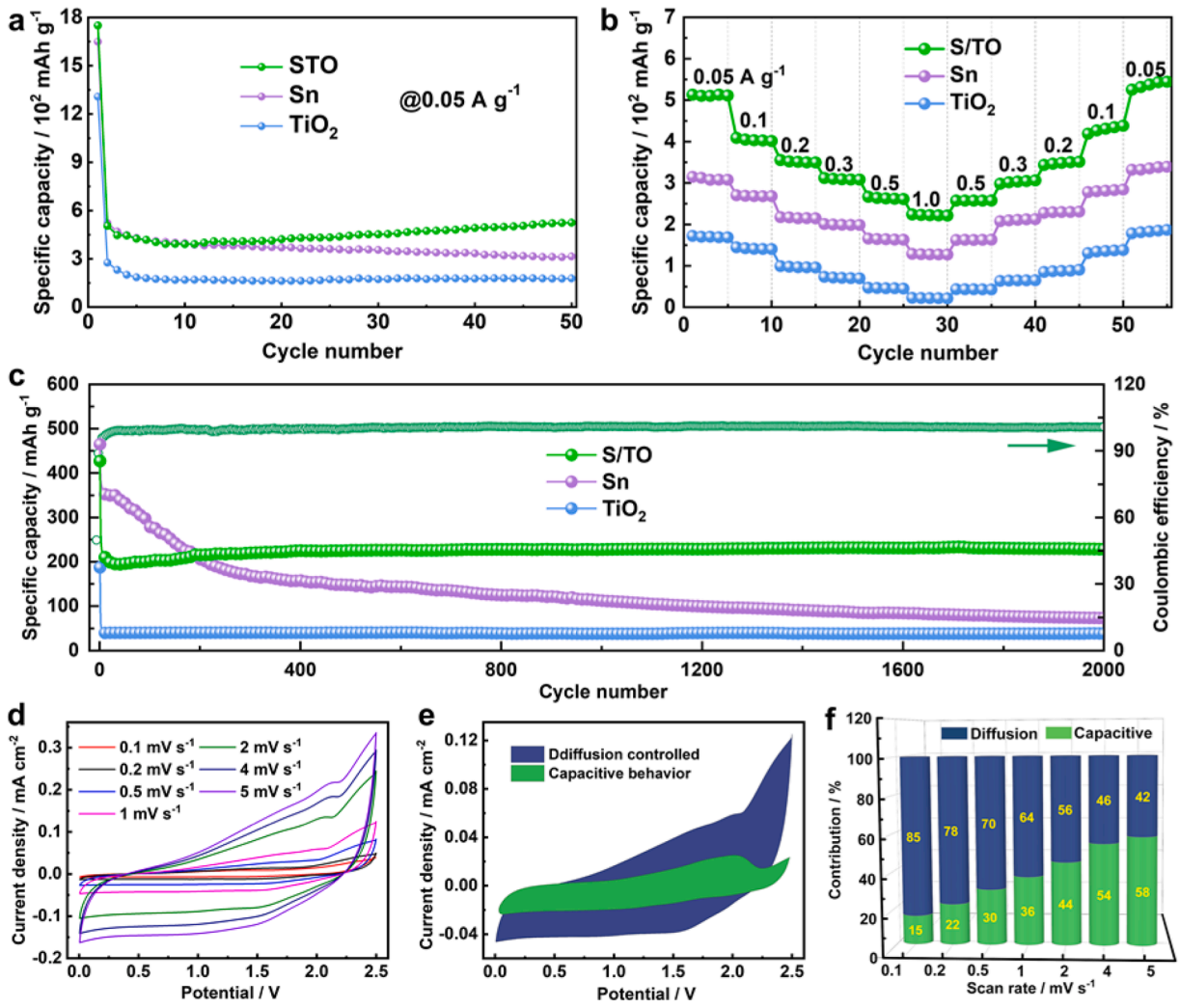

Fig. 4. Electrochemistry of S/TO heterojunctions. (a) Cycling profiles at 0.05 A g^{-1}, (b) rate capability, (c) long term cycling stability at 1.0 A g^{-1} of S/TO heterojunctions. (d) CV curves of S/TO at various scan rates, (e) diffusion- and capacitance-controlled contributions to the total capacity at 1 mV s^{-1}, (f) normalized contribution ratios at different scan rates of S/TO heterojunctions.

were studied by cyclic voltammetry (CV) test with scan rates from 0.1 to 5 mV s^{-1}. The CV profiles exhibit a linear dependence of current density versus the scan rates (Fig. 4d). There exists a relationship between the current (i) and the scan rate (ν) $i = a\nu^b$, where a and b are indexed as the fitting parameters [42]. The b values of 0.5 and 1.0 are refer to diffusion- and surface-directed energy storage processes, respectively [42]. By plotting log$i$ *v.s.* logν, the b values at various potentials are determined to be between 0.8 and 1.0 which means that the specific capacity of S/TO is contributed by both diffusion- and surface-controlled processes (Figures S21–22). Moreover, the ratio of capacitive contribution increases as the scan rates increases. The green region shows a pseudocapacitive contribution of 36 % for the S/TO heterostructures at 1.0 mV s^{-1} as shown in Fig. 4e,f. Such an obvious coexistence of storage and surface adsorption of Na^+ ion makes the S/TO electrode capable of balancing the energy and power densities in building better SIBs.

2.3. Sodium storage mechanism in the S/TO superlattice electrode

To study the sodium storage mechanism, *in-situ* XRD experiments are firstly performed to examine the structural changes of the S/TO electrode upon the sodiation/desodiation process (Fig. 5a and S23–24). From the XRD patterns, the (200), (101), (220) and (211) peaks of Sn nanocrystals attenuate gradually as discharge proceeds, corresponding to the pulverization of Sn electrode, the generation of Na_xSn alloys and some other intermediates (e. g. Na_2O) upon sodiation of Sn with the inserted Na and electrolyte. Then, most of these newly formed XRD peaks grow gradually in the following charge process, to demonstrate the progressive reaction of Na with the Sn component in the S/TO electrode. Moreover, there exists an intense peak at 19.7° shifting negatively to 19.1° in the late discharge process, which accounts for the transformation of Na_9Sn_4 to $Na_{15}Sn_4$ by further sodiation [41]. In contrast, these intermediate phases disappear at the end of charge and the XRD peaks of Sn nanocrystals recover back again as shown in Fig. 5a. This is a typical evidence for the Na-Sn alloying process. Then for the TiO_2 component, no obvious XRD peak change of (200) plane is witnessed to demonstrate the solid-solution reaction with very limited volume variation upon Na exchange with TiO_2 nanocrystal electrode. As a matter of fact, the repeated *in-situ* XRD results of S/TO electrode with long cycling life span evidences strongly the spatial confinement effect in this periodic nanostructured electrode for energy storage and conversion applications, where the nanosizing and pulverization of Sn particles is effectively space-limited in between the TiO_2 slabs and the notorious catalytic reaction between electrolyte and TiO_2 surface region is sophisticatedly saturated by the Sn-O-Ti interfacial connections as well as the electron accumulation in TiO_2 as shown in Fig. 3, 4e and 5a, synergistically elevating the Na storage and transport performance of the S/TO electrode as exhibited in Fig. 4. This is also the fantastic aspect to overcome the intrinsic disadvantages of single material using the

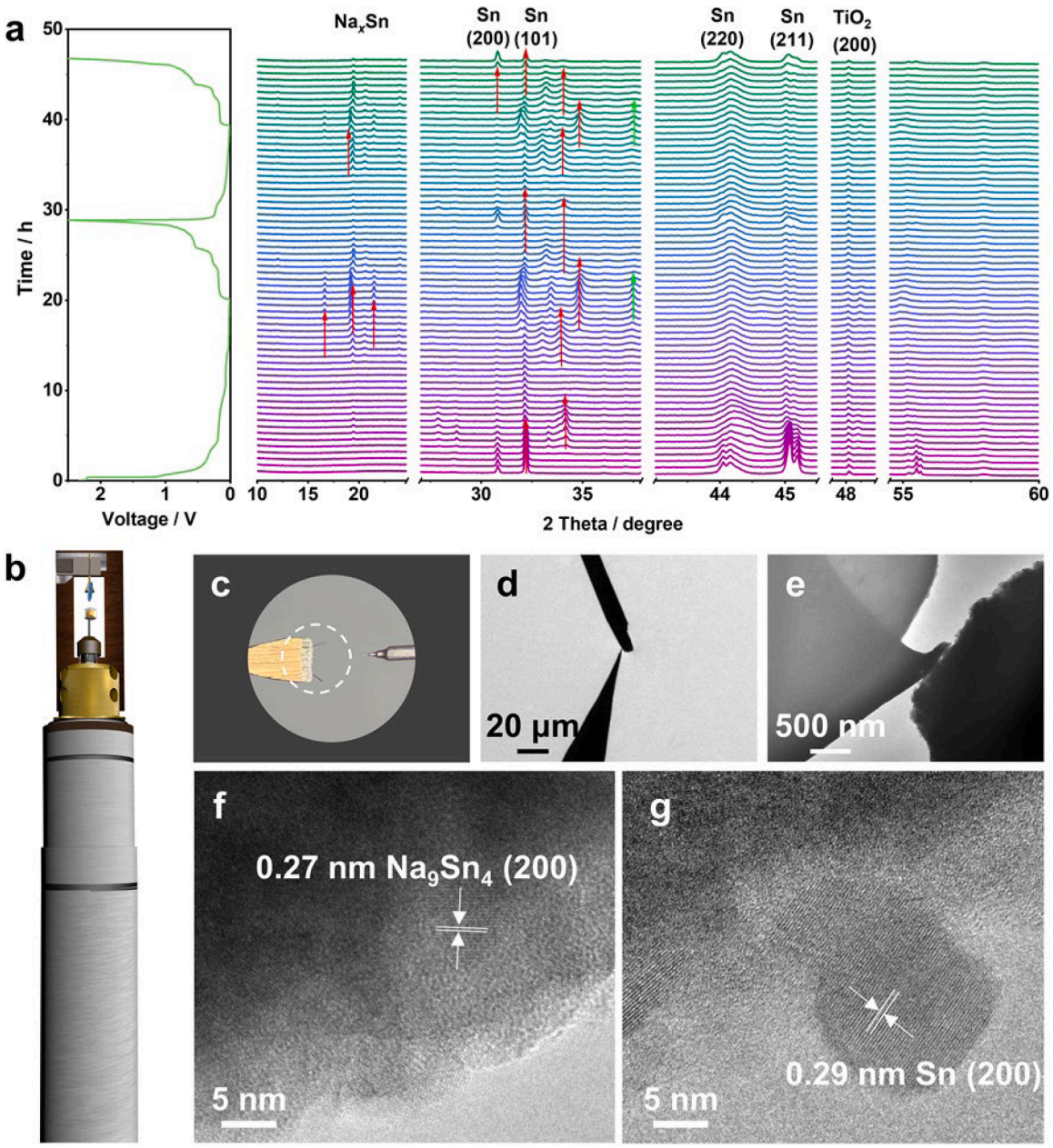

Fig. 5. *In-situ* structural and morphological changes of the S/TO heterojunctions. (a) *In-situ* XRD results, and (b, c) *in-situ* TEM setup. (d, e) The sodium coated tungsten probe and S/TO electrode contact with the zoom in observation. (f, g) TEM observation of the cycled S/TO electrode.

heterostructure electrochemistry to develop high-performance composite electrodes at present.

What's more, the *in-situ* TEM experiment is further performed to inspect the structural and morphological changes of the S/TO electrode as shown in Fig. 5b-g. The S/TO thin films and sodium foil are fixed on a gold wedge and a tungsten probe as the working and the reference electrodes, respectively (Fig. 5b, S25). Then negative and positive biases are exerted to carry out sodiation and desodiation processes (Figure S26). From TEM observations, the Na_9Sn_4 intermediate is detected with a lattice *d*-spacing of 0.27 nm in the discharged S/TO electrode, in consistence with the reported value (Fig. 5f) [43]. While in the charged S/TO electrode (Fig. 5g), a lattice fringe value of 0.29 nm can be identified to be Sn (200) plane [44], in line with above *in-situ* XRD results and to verify the reversibility of the S/TO thin film electrode.

Fig. 6 presents the atomic-scale working process of the S/TO heterojunctions. From the calculated charge density difference (CDD) at the atomic interface of the S/TO heterostructures, Sn-O-Ti interfacial bonds are generated upon the formation of heterojunctions and the charge transfers from Sn to TiO_2, inducing the partial reduction of surficial TiO_2 (Fig. 6a). Consequently, the TiO_2 and Sn become electron-rich domains and electron-deficient domains, respectively (Fig. 6b), which creates BIEFs pointing from Sn to TiO_2, in line with the SKPM results as shown in Fig. 3d. Further simulation results indicate the most likely Na^+ ion diffusion pathway is long the [001] direction in the S/TO heterojunctions. As can be seen from Fig. 6c-e and S27, when the number of intercalated Na^+ ion increases from one to six, the negative free energies mean that Na^+ ion intercalation at the heterointerface is a thermodynamic-allowed spontaneous process and the heterointerfaces provide extra space and active sites for sodium storage with respect to TiO_2 or Sn. Furthermore, upon Na^+ insertion, the formation energy of capturing the first four Na^+ ions increase gradually while the subsequent Na^+ accumulation leads to the breakage of the Ti-O-Sn interfacial bond to decrease the formation energy as shown in Figure S27. As a matter of fact, the BIEFs originate from the different chemical potentials (μ, or

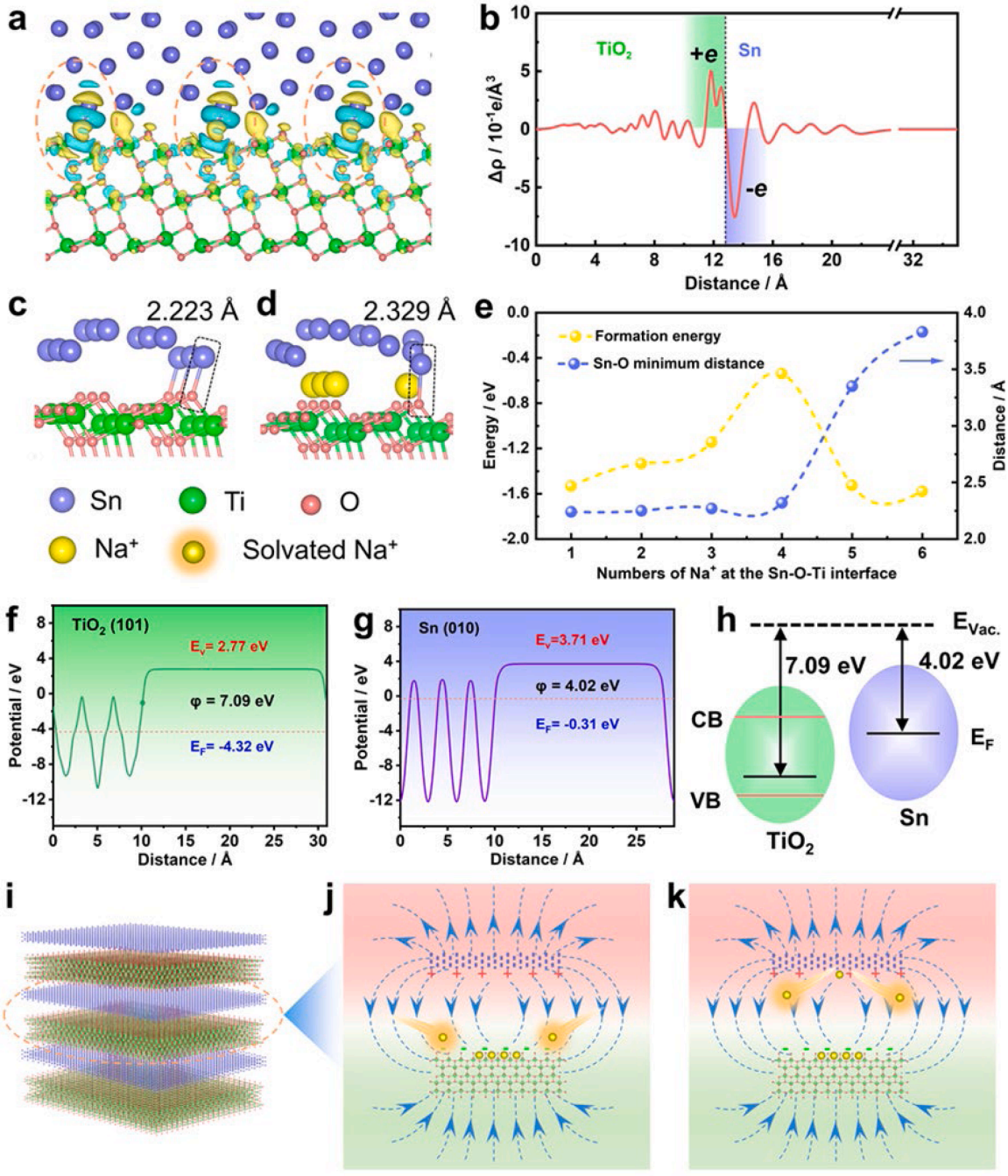

Fig. 6. Atomic scale working process of S/TO heterojunctions. (a) Charge density difference and (b) planar-average electron density difference at the interface of S/TO superlattice heterostructures. (c, d) DFT simulations of the pristine S/TO and the discharged state with four sodium ions. (e) Formation energies and minimum Sn-O distances as a function of the interfacial sodium ions. (f-h) Work function analyses of TiO_2 and Sn. (i-k) Schematic illustration on sodium storage in the S/TO superlattice heterojunctions.

Femi levels E_F) of two building blocks. The work functions (ϕ, equal to E_v-E_F where the E_v corresponds to the vacuum energy level) of TiO_2 and Sn are calculated to be 8.03 and 4.02 eV, respectively (Fig. 6f, g). Such a big difference in ϕ inevitably stimulates the electronic redistribution during band alignment at the heterointerface between TiO_2 and Sn as shown in Fig. 6h. The electrons from the high Femi-level Sn will spontaneously flow to the low Femi-level TiO_2 to build BIEFs at the interfaces, which agrees with the CDD results (Fig. 6a, b). According to the projected electronic density of states (DOS) as presented in Figure S28, the Sn and TiO_2 present typical metallic and semiconductor properties, respectively. For the S/TO heterostructures, the disparate Femi levels prompt charge redistribution at the interface until the Femi levels of these components achieve the equilibrium accompanied by the disappearance of holes filled with electrons near the Femi level of TiO_2, which is also in line with the CDD results displayed in Fig. 6a, b.

Based on aforementioned analyses, Fig. 6i-k schematically demonstrates the sodium storage mechanism together with the functional behaviors of BIEFs inside the S/TO heterojunctions during electrochemical cycling. The TiO_2 component possesses a higher sodium intercalation potential than that of Sn part, so it will firstly capture Na^+ ion during discharging, the electronic and ionic movements of which would be accelerated by the BIEFs pointed from Sn to TiO_2 inside the

heterostructures. As there exists a huge work function (ϕ) difference between Sn and TiO_2, the BIEFs (~ 10^3 V/m) maintain the same direction during cycling. On the other hand, since the desodiation potential of Sn is lower than that of TiO_2, the Na^+ ions will be firstly detached from Sn and also significantly accelerated by the BIEFs. In brief, the direction of BIEFs remains unchanged so that BIEFs facilitate the sodiation at the TiO_2 side and initiate the desodiation from the Sn side, in line with their theoretical (de)intercalation potentials to co-contribute to the outstanding electrochemical performance of the S/TO electrode.

3. Conclusion

In summary, we have demonstrated a rational design of S/TO superlattice heterojunctions thin films with BIEFs at the atomic interfaces via an effective strain-release approach. Such vertical superlattice heterostructures contributed to the optimized band structure, more accessible interface, enhanced adsorption energy and restrained volume expansion, which integrates the merits of complementary Sn and TiO_2 and overcome their shortcomings. More importantly, the interfacial BIEFs constructed from the work function difference expedite electron and ionic transfer, thus greatly lowering the formation energy of sodium ion storage. Our work illustrates an effective approach to tailor the structural and electrochemical properties of electrode materials by interface engineering and provides insights into the functional mechanism of BIEFs for sodium ion storage.

4. Experimental section

4.1. Synthesis of S/TO thin film heterostructures

The S/TO was prepared by a self-rolling process. First of all, the sacrificial photoresist layer was spin-coated onto an Al foil substrate with a speed of 4500 rpm, followed by baking on a hotplate for 1 min to remove the residue solvent. After that, Sn and TiO_2 thin films were sequentially deposited onto the PMMA layer. Then the substrate coated with thin films was immersed into isopropanol to selectively remove the sacrificial layer, which induced the self-rolling of hybrid thin films and detachment from the substrate. Finally, the thin films were dried by a CO_2 super critical point dryer. For comparison, pure Sn and TiO_2 thin films were also prepared using the same method.

4.2. Characterizations

The morphology of thin films was characterized by SEM (Zeiss Gemini 300) at an acceleration voltage of 10 kV. The detailed microstructure and composition were examined by TEM (FEI Helios NanoLab 450S) at 200 kV and aberration-corrected TEM (AC-STEM, FEI Titan ChemisSTEM 80–300) at 300 kV. Before the analysis, the FIB-derived lamella was treated with O_2/Ar plasma for 10 s. For the SKPM measurement (Bruker Dimension ICON), a TiO_2 thin film was firstly deposited on the Si substrate and then it was coated by a patterned photoresist through optical lithography which was then removed after the Sn thin film was deposited onto the TiO_2, thus forming a stepped TiO_2/Sn heterostructure on the substrate. The surficial components and chemical state of thin films were inspected by XPS (Thermo Scientific K-Alpha). The materials were also identified by powder XRD (Bruker D8 Advance) with Cu Kα radiation operated at 40 kV and 40 mA.

4.3. Electrochemical measurements

The sodium-ion battery performance was investigated using coin-type cells assembled in an Ar-filled glove box. The working electrode was prepared by mixing thin film powders, acetylene black and polyvinylidene difluoride (PVDF) with a mass ratio of 70:20:10 in N-methyl pyrrolidone via vibration instead of ultrasonication to keep the intact structure. Homogeneous slurry was prepared after vibration for 6 h which was then spread onto an Al foil and dried in a vacuum oven overnight. The mass loading of each disc was ~1.0 mg cm^{-2}. The sodium ion batteries were assembled using the as-prepared electrode disc as the working electrode and a piece of sodium foil as the counter electrode and reference electrode. The electrolyte consists of 1 M $NaPF_6$ in dimethyl carbonate (DEC)-ethylene carbonate (EC) (1:1 Vol%). Glassy fiber (Whatman GF/D) was employed as the separator. The cells were galvanostatically discharged/charged by Land CT2001A battery test system. The cyclic voltammetry was carried out on PGSTAT302N.

4.4. Theoretical calculation

All spin-polarized total energy calculations were performed using the Vienna Ab Initio Simulation Package (VASP) within the projector augmented wave (PAW) method based on density functional theory (DFT) [45,46]. The generalized gradient approximation (GGA) was used to describe the electron-electron exchange correlations in the parameterization of Perdew, Burke, and Ernzerhof (PBE) [47]. A plane wave representation for the wave function with a cutoff energy of 500 eV was applied. A gamma-centered K-point mesh of 0.04 $Å^{-1}$ was used for the Brillouin zone sampling. Geometry optimizations were performed until all the forces acting on ions were less than 0.03 eV/Å. The crystal structures and charge density were visualized using the VESTA software. The large enough extended supercell was adopted to build the TiO_2 (101)/Sn (010) heterojunction for electronic structure as well as kinetics simulations, which contains 144 atoms (108 atoms for TiO_2 and 36 atoms for metal Sn, respectively).

CRediT authorship contribution statement

Xueyi Lu: Writing – original draft, Investigation, Funding acquisition, Formal analysis, Data curation, Conceptualization. **Weixin Chen:** Writing – original draft, Methodology, Formal analysis. **Jianfang Yang:** Writing – review & editing, Formal analysis. **Xuemin Wu:** Formal analysis. **Yan Wang:** Writing – review & editing, Formal analysis. **Oliver G. Schmidt:** Writing – review & editing, Formal analysis. **Lifeng Liu:** Writing – review & editing, Investigation, Formal analysis. **Daiming Tang:** Writing – review & editing, Methodology, Investigation, Formal analysis. **Xia Lu:** Writing – review & editing, Supervision, Funding acquisition, Formal analysis.

Declaration of competing interest

The authors declare that they have no known competing financial interests or personal relationships that could have appeared to influence the work reported in this paper.

Acknowledgements

This work was supported by National Natural Science Foundation of China (22209213, 22379168), Natural Science Foundation of Guangdong Province (2022A1515010405, 2024A1515010284), and the Foundation from Guangdong Provincial Key Laboratory of Materials and Technologies for Energy Conversion (MATEC2023KF004). The authors acknowledge Shiyanjia Lab for the XPS analysis.

Supplementary materials

Supplementary material associated with this article can be found, in the online version, at doi:10.1016/j.ensm.2025.104112.

Data availability

Data will be made available on request.

References

[1] Q. Wang, Z. Yao, J. Wang, H. Guo, C. Li, D. Zhou, X. Bai, H. Li, B. Li, M. Wagemaker, C. Zhao, Chemical short-range disorder in lithium oxide cathodes, Nature 629 (2024) 341–347.

[2] X. Wang, Q. Zhang, C. Zhao, H. Li, B. Zhang, G. Zeng, Y. Tang, Z. Huang, I. Hwang, H. Zhang, S. Zhou, Y. Qiu, Y. Xiao, J. Cabana, C. Sun, K. Amine, Y. Sun, Q. Wang, G. Xu, L. Gu, Y. Qiao, S. Sun, Achieving a high-performance sodium-ion pouch cell by regulating intergrowth structures in a layered oxide cathode with anionic redox, Nat. Energy 9 (2024) 184–196.

[3] W. Feng, C. Meng, X. Guo, B. Wu, X. Sui, Z. Wang, Defect-driven reconstruction of Na-ion diffusion channels enabling high-performance Co-doped TiO_2 anodes for Na-ion hybrid capacitors, Adv. Energy Mater. 14 (2024) 2400558.

[4] C. Zhao, Q. Wang, Z. Yao, J. Wang, B. Sánchez-Lengeling, F. Ding, X. Qi, Y. Lu, X. Bai, B. Li, H. Li, A. Aspuru-Guzik, X. Huang, C. Delmas, M. Wagemaker, L. Chen, Y. Hu, Rational design of layered oxide materials for sodium-ion batteries, Science 370 (2020) 708–711.

[5] Y. Shi, F. Geng, Y. Sun, P. Jiang, W.H. Kan, W. Tong, X. Lu, G. Qian, N. Zhang, B. Wei, B. Hu, D. Cao, X. Lu, Sustainable anionic redox by inhibiting Li cross-layer migration in Na-based layered oxide cathodes, ACS Nano 18 (2024) 5609–5621.

[6] J. Liu, Z. Ni, C. Wei, Z. Wang, S. Liu, H. Zhang, C. Yang, S. Xiong, J. Feng, Advanced electrolytes for sodium metal batteries under extreme conditions, Energy Storage Mater 72 (2024) 103753.

[7] Y. Shi, P. Jiang, S. Wang, W. Chen, B. Wei, X. Lu, G. Qian, W.H. Kan, H. Chen, W. Yin, Y. Sun, X. Lu, Slight compositional variation-induced structural disorder-to-order transition enables fast Na^+ storage in layered transition metal oxides, Nat. Commun. 13 (2022) 7888.

[8] S. Qiao, Q. Zhou, M. Ma, H.K. Liu, S.X. Dou, S. Chong, Advanced anode materials for rechargeable sodium-ion batteries, ACS Nano 17 (2023) 11220–11252.

[9] S. Liang, Y.-J. Cheng, J. Zhu, Y. Xia, P. Müller-Buschbaum, A chronicle review of nonsilicon (Sn, Sb, Ge)-based lithium/sodium-ion battery alloying anodes, Small Methods 4 (2020) 2000218.

[10] C. Wu, G. Zhu, Q. Wang, M. Wu, H. Zhang, Sn-based nanomaterials: from composition and structural design to their electrochemical performances for Li- and Na-ion batteries, Energy Storage Mater 43 (2021) 430–462.

[11] J. Sun, H.W. Lee, M. Pasta, H. Yuan, G. Zheng, Y. Sun, Y. Li, Y. Cui, A phosphorene-graphene hybrid material as a high-capacity anode for sodium-ion batteries, Nat. Nanotechnol. 10 (2015) 980–985.

[12] J. Cao, L. Wang, D. Li, Z. Yuan, H. Xu, J. Li, R. Chen, V. Shulga, G. Shen, W. Han, $Ti_3C_2T_x$ MXene conductive layers supported bio-derived $Fe_{x-1}Se_x$/MXene/carbonaceous nanoribbons for high-performance half/full sodium-ion and potassium-ion batteries, Adv. Mater. 33 (2021) 2101535.

[13] L. Shen, Y. Wang, H. Lv, S. Chen, P.A. Aken, X. Wu, J. Maier, Y. Yu, Ultrathin $Ti_2Nb_2O_9$ nanosheets with pseudocapacitive properties as superior anode for sodium-ion batteries, Adv. Mater. 30 (2018) 1804378.

[14] X. Lu, Y. Shi, D. Tang, X. Lu, Z. Wang, N. Sakai, Y. Ebina, T. Taniguchi, R. Ma, T. Sasaki, C. Yan, Accelerated ionic and charge transfer through atomic interfacial electric fields for superior sodium storage, ACS Nano 16 (2022) 4775–4785.

[15] R. Usiskin, Y. Lu, J. Popovic, M. Law, P. Balaya, Y. Hu, J. Maier, Fundamentals, status and promise of sodium-based batteries, Nat. Rew. Mater. 6 (2021) 1020–1035.

[16] X. Ou, L. Cao, X. Liang, F. Zheng, H.-S. Zheng, X. Yang, J.-H. Wang, C. Yang, M. Liu, Fabrication of SnS_2/Mn_2SnS_4/carbon heterostructures for sodium-ion batteries with high initial coulombic efficiency and cycling stability, ACS Nano 13 (2019) 3666–3676.

[17] Q. Wei, X. Chang, D. Butts, R. DeBlock, K. Lan, J. Li, D. Chao, D.-L. Peng, B. Dunn, Surface-redox sodium-ion storage in anatase titanium oxide, Nat. Commun. 14 (2023) 7.

[18] F. Zhang, J. Zhu, D. Zhang, U. Schwingenschlögl, H.N. Alshareef, Two-dimensional SnO anodes with a tunable number of atomic layers for sodium Ion batteries, Nano Lett 17 (2017) 1302–1311.

[19] H. Qiu, L. Zhao, M. Asif, X. Huang, T. Tang, W. Li, T. Zhang, T. Shen, Y. Hou, SnO_2 nanoparticles anchored on carbon foam as a freestanding anode for high performance potassium-ion batteries, Energy Environ. Sci. 13 (2020) 571–578.

[20] S. Wang, S. Zhao, X. Guo, G. Wang, 2D material-based heterostructures for rechargeable batteries, Adv. Energy Mater. 12 (2022) 2100864.

[21] T. Wang, P. Wang, W. Zang, X. Li, D. Chen, Z. Kou, S. Mu, J. Wang, Nanoframes of Co_3O_4-Mo_2N heterointerfaces enable high-performance bifunctionality toward both electrocatalytic HER and OER, Adv. Funct. Mater. 32 (2021) 2107382.

[22] S. Li, Y. Liu, X. Zhao, Q. Shen, W. Zhao, Q. Tan, N. Zhang, P. Li, L. Jiao, X. Qu, Sandwich-like heterostructures of MoS_2/graphene with enlarged interlayer spacing and enhanced hydrophilicity as high-performance cathodes for aqueous zinc-ion batteries, Adv. Mater. 33 (2021) 2007480.

[23] E. Pomerantseva, Y. Gogotsi, Two-dimensional heterostructures for energy storage, Nat. Energy 2 (2017) 17089.

[24] J. Ding, H. Li, S. Wang, S. Wu, L. Zhang, L. Zhou, S. Fang, Y. Yu, Vertical two-dimensional heterostructures and superlattices for lithium batteries and beyond, Nano Energy 129 (2024) 110042.

[25] X. Guo, W. Zhang, J. Zhang, D. Zhou, X. Tang, X. Xu, B. Li, H. Liu, G. Wang, Boosting sodium storage in two-dimensional Phosphorene/$Ti_3C_2T_x$ MXene nanoarchitectures with stable fluorinated interphase, ACS Nano 14 (2020) 3651–3659.

[26] P. Xiong, X. Zhang, F. Zhang, D. Yi, J. Zhang, B. Sun, H. Tian, D. Shanmukaraj, T. Rojo, M. Armand, R. Ma, T. Sasaki, G. Wang, Two-dimensional unilamellar cation-deficient metal oxide nanosheet superlattices for high-rate sodium ion energy storage, ACS Nano 12 (2018) 12337–12346.

[27] Y. Liu, Y. Huang, X. Duan, Van der Waals integration before and beyond two-dimensional materials, Nature 567 (2019) 323–333.

[28] J. Ni, M. Sun, L. Li, Highly efficient sodium storage in iron oxide nanotube arrays enabled by built-in electric field, Adv. Mater. 31 (2019) 1902603.

[29] Y. Li, J. Zhang, Q. Chen, X. Xia, M. Chen, Emerging of heterostructure materials in energy storage: a review, Adv. Mater. 33 (2021) 2100855.

[30] J. Deng, X. Lu, L. Liu, L. Zhang, O.G. Schmidt, Introducing rolled-up nanotechnology for advanced energy storage devices, Adv. Energy Mater. 6 (2016) 1600797.

[31] L. Zhang, J. Deng, L. Liu, W. Si, S. Oswald, L. Xi, M. Kundu, G. Ma, T. Gemming, S. Baunack, F. Ding, C. Yan, O.G. Schmidt, Hierarchically designed SiO_x/SiO_y bilayer nanomembranes as stable anodes for lithium ion batteries, Adv. Mater. 26 (2014) 4527–4532.

[32] H.-X. Ji, X.-L. Wu, L.-Z. Fan, C. Krien, I. Fiering, Y.-G. Guo, Y. Mei, O.G. Schmidt, Self-wound composite nanomembranes as electrode materials for lithium ion batteries, Adv. Mater. 22 (2010) 4591–4595.

[33] X. Lu, Y. Yang, Y. Yin, Z. Wang, L. Sutrisno, C. Yan, O.G. Schmidt, Atomic heterointerface boosts the catalytic activity toward oxygen reduction/evolution reaction, Adv. Energy Mater. 11 (2021) 2102235.

[34] O.G. Schmidt, K. Eberl, Thin solid films roll up into nanotubes, Nature 410 (2001) 168.

[35] Y. Mei, G. Huang, A.A. Solovev, E.B. Ureña, I. Mönch, F. Ding, T. Reindl, R.K.Y. Fu, P.K. Chu, O.G. Schmidt, Versatile approach for integrative and functionalized tubes by strain engineering of nanomembranes on polymers, Adv. Mater. 20 (2008) 4085–4090.

[36] L. Chu, Z. Qin, J. Yang, X.a. Li, Anatase TiO_2 nanoparticles with exposed {001} facets for efficient dye-sensitized solar cells, Sci. Rep. 5 (2015) 12143.

[37] NIST X-ray Photoelectron Spectroscopy Database, National Institute of Standards and Technology, Gaithersburg MD, 2000, p. 20899.

[38] C. Di Valentin, G. Pacchioni, A. Selloni, Electronic structure of defect states in hydroxylated and reduced rutile TiO_2 (110) Surfaces, Phys. Rev. Lett. 97 (2006) 166803.

[39] X. Lu, L. Gu, Y.-S. Hu, H.-C. Chiu, H. Li, G.P. Demopoulos, L. Chen, New insight into the atomic-scale bulk and surface structure evolution of $Li_4Ti_5O_{12}$ anode, J. Am. Chem. Soc. 137 (2015) 1581–1586.

[40] H. He, Q. Gan, H. Wang, G.-L. Xu, X. Zhang, D. Huang, F. Fu, Y. Tang, K. Amine, M. Shao, Structure-dependent performance of TiO_2/C as anode material for Na-ion batteries, Nano Energy 44 (2018) 217–227.

[41] Z. Li, J. Ding, D. Mitlin, Tin and tin compounds for sodium ion battery anodes: phase transformations and performance, Acc. Chem. Res. 48 (2015) 1657–1665.

[42] D. Chao, C. Zhu, P. Yang, X. Xia, J. Liu, J. Wang, X. Fan, S.V. Savilov, J. Lin, H. J. Fan, Z.X. Shen, Array of nanosheets render ultrafast and high-capacity Na-ion storage by tunable pseudocapacitance, Nat. Commun. 7 (2016) 12122.

[43] G. Deysher, Y.-T. Chen, B. Sayahpour, S.W.-H. Lin, S.-Y. Ham, P. Ridley, A. Cronk, E.A. Wu, D.H.S. Tan, J.-M. Doux, J.A.S. Oh, J. Jang, L.H.B. Nguyen, Y.S. Meng, Evaluating electrolyte–anode interface stability in sodium all-solid-state batteries, ACS Appl. Mater. Interfaces 14 (2022) 47706–47715.

[44] X. Li, W. Li, Z. Miao, C. Lu, H. Ma, Y. Xu, D. Gong, C.-Y. Xu, Z. Zha, Liquid exfoliation of stanene as degradable nanoagents for NIR-II photothermal therapy, J. Mater. Sci. Technol. 148 (2023) 186–198.

[45] G. Kresse, J. Furthmüller, Efficient iterative schemes for ab initio total-energy calculations using a plane-wave basis set, Phys. Rev. B 54 (1996) 11169–11186.

[46] P.E. Blöchl, Projector augmented-wave method, Phys. Rev. B 50 (1994) 17953–17979.

[47] J.P. Perdew, K. Burke, M. Ernzerhof, Generalized gradient approximation made simple, Phys. Rev. Lett. 77 (1996) 3865–3868.